



ELSEVIER

Contents lists available at ScienceDirect

## Journal of Magnetism and Magnetic Materials

journal homepage: [www.elsevier.com/locate/jmmm](http://www.elsevier.com/locate/jmmm)

## Research articles

## Ferrofluidic Taylor Couette flow in between finite length porous cylinders with radial through-flow

Sebastian Altmeyer

Castelldefels School of Telecom and Aerospace Engineering, Universitat Politècnica de Catalunya, 08034 Barcelona, Spain

## A B S T R A C T

We study ferrofluidic Taylor Couette flow under the influence of radial inflow and outflow in combination with an external applied magnetic field in a finite-length cavity via direct numerical simulations. As is the case for no magnetic field, the base state (cylindrical Couette flow and modified circular-Couette flow in presence of a transverse magnetic field component, respectively) with an external magnetic field is stabilized for any radial inflow and strong radial outflow, while the system becomes slightly destabilized for weak radial outflow. The particular parameter range for destabilization depends on the field strength of the applied magnetic field. Slightly increasing the field strength shrinks the range, while it grows for larger field strengths. In general, a larger field strength tends to minimize and compensate the effect of any radial flow, resulting in bifurcation thresholds (critical Reynolds number vs. radial flow) which have less curvature, i.e. they are more flat. We elucidate the origin of this effect to be in the symmetry breaking nature of the transverse magnetic field itself. Azimuthal velocity isocontours are shifted different strong due to radial flow, either in the part of the annulus that is aligned with the direction of the applied magnetic field or perpendicular to it. In particular, the modulation amplitude in the isocontours perpendicular to the field increase. As a result the flow is locally stabilized with different strength, so that the overall stabilization is weaker relative to the situation without any applied field. This diminishing curvature effect with variation of the radial flow becomes more pronounced with stronger applied magnetic fields.

## 1. Introduction

The flow between two concentric cylinders driven by differential rotation, Taylor-Couette flow, has played a paradigmatic role for the development of hydrodynamic stability theory [1] and testing applications of low dynamical system theory [2]. The geometric simplicity allows for well-controlled experiments that allow verification of numerical simulations, which together shed light on hydrodynamic stability and the transition to turbulence.

In absence of any magnetic field, the stable azimuthal circular Couette flow (CCF) of a Newtonian fluid between a rotating inner cylinder and a stationary outer cylinder becomes centrifugally unstable upon exceeding a critical rotation speed. The result is the appearance of axisymmetric toroidal closed Taylor vortices, typically called Taylor vortex flow (TVF) [1]. However, the critical values for the appearance of these vortex structures depend on various parameters that can be altered in several ways. For instance, if both cylinders are permeable and a radial through-flow is imposed through them, the system stability changes. Based on linear stability analysis for axisymmetric disturbances, the flow is stabilized by a radial inward flow or strong radial outward flow, while a weak radial outward flow destabilizes the system slightly [3–9].

Another situation in which the stability can be altered is by considering non-ordinary fluids such as ferrofluids [10], which are fluids

consisting of a dispersion of magnetized nanoparticles in a variety of liquid carriers that are stabilized against particle agglomeration through the addition of a surfactant monolayer on the particles. In the absence of any magnetic field, the nanoparticles are randomly oriented so that the fluid has zero net magnetization. In this case, the nanoparticles alter the viscosity and the density of the fluid very little. Thus, in the absence of any external field a ferrofluid behaves as an ordinary (classical) Newtonian fluid. However, when a magnetic field of sufficient strength is applied, the hydrodynamical properties of the fluid, such as the viscosity, can change dramatically [11–14], resulting in very different dynamics.

The magnetoviscous effect in ferrofluids is highly dependent on the orientation of the magnetic field with respect to the fluid flow [15]. Under a symmetry-breaking transverse magnetic field, all flow states in the Taylor-Couette system (TCS) become intrinsically three-dimensional [16–18], increasing the already large number of flow states known to exist in the system [1,2,19–22]. Any external applied magnetic field results in a general stabilization of the basic state as well as shifting bifurcation thresholds for any flow structure. If the external applied magnetic field is either axial, radial or azimuthal orientated, its orientation does not play any role qualitatively. Only quantitative differences in the distance of the up-shift of primary bifurcation thresholds can be detected [13,14,16–18,23,24]. However, it is crucial to note that the presence of a transversal magnetic field alters the classical

E-mail address: [sebastian.altmeyer@t-online.de](mailto:sebastian.altmeyer@t-online.de).

<https://doi.org/10.1016/j.jmmm.2019.166363>

Received 20 August 2019; Received in revised form 25 December 2019; Accepted 27 December 2019

Available online 30 December 2019

0304-8853/ © 2019 Elsevier B.V. All rights reserved.

symmetries in TCS. The classical TCS, where a Newtonian fluid is confined by end walls, is invariant to arbitrary rotations  $R_\alpha$  about the axis and the reflections  $K_z$  about axial mid-height, and time translations  $\Phi_{t_0}$ , generating the symmetry group  $SO(2) \times Z_2 \times \mathbf{R}$ . Here the first two factors consist of the purely spatial symmetries, while the third factor corresponds to the temporal symmetries generating the one-dimensional translation group  $\mathbf{R}$ . Under an imposed transverse magnetic field, these symmetries are broken and the flow is inherently *three-dimensional* for any nonzero flow and magnetic field such that only a single finite mode contribution is stimulated [14]. Thus, the resultant flow has even more complex symmetries [18,25]. There is a reflection  $K_z^H$  about the annulus' mid-height plane that occurs with an inversion of the magnetic field direction. In addition, there is a rotation invariance  $R_\alpha^H$  for discrete angle along with an inversion of the magnetic-field direction with the angle  $\pi$  being aligned with the direction that the magnetic field enters the annulus.

Here we consider the interaction of two mechanisms, the magnetic field interaction with a ferrofluid and a radial through-flow, to provides new insight for various situations such as rotating filtration. The basis for rotating filtration is a radial flow at a permeable inner cylinder of a Taylor-Couette cell [26]. Rotating filtration is widely used commercially for extracting plasma from whole blood [27–29]. The approach has also been proposed as a method for other filtration applications as well [30–38]. Although a radial through-flow between two porous cylinders is somewhat different from rotating filtration in which the outer cylinder is non-porous, it can provide insight into the fundamental mechanisms that alter the stability of Taylor-Couette flow when a radial flow is present. To our knowledge this paper represents the first investigation of the interaction between a radial imposed through-flow and an externally applied magnetic field on a ferro-fluid in the Taylor-Couette geometry.

## 2. System parameters and the Navier–Stokes equation

We consider a standard TCS (Fig. 1) consisting of two concentric, independently rotating cylinders. Within the gap between the two cylinders is an incompressible, isothermal, homogeneous, Newtonian, mono-disperse ferrofluid of kinematic viscosity  $\nu$  and density  $\rho$ . The inner and outer cylinders have radii  $R_i$  and  $R_o$ , and the inner cylinder rotates with angular velocity  $\omega_i$  while the outer one is stationary. We consider no-slip rigid (stationary) boundary conditions (RBC) at the endwalls as well as periodic boundary conditions (PBC) instead of

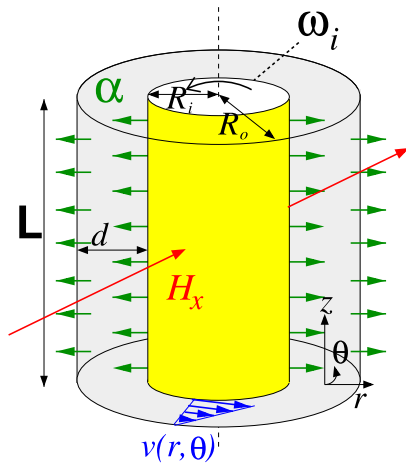


**Fig. 1.** Taylor-Couette system. Schematic of the Taylor-Couette system (TCS) illustrating radial flow and an externally applied homogeneous magnetic field  $\mathbf{H}_{ext} = H_x \hat{\mathbf{e}}_x$ . The stable Couette velocity profile  $v(r, \theta)$  is shown (not to scale). The radial flow at the permeable walls of the concentric cylinders can be outward ( $\alpha > 0$ ), as shown, or inward ( $\alpha < 0$ ). The used coordinate system is illustrated at bottom right.

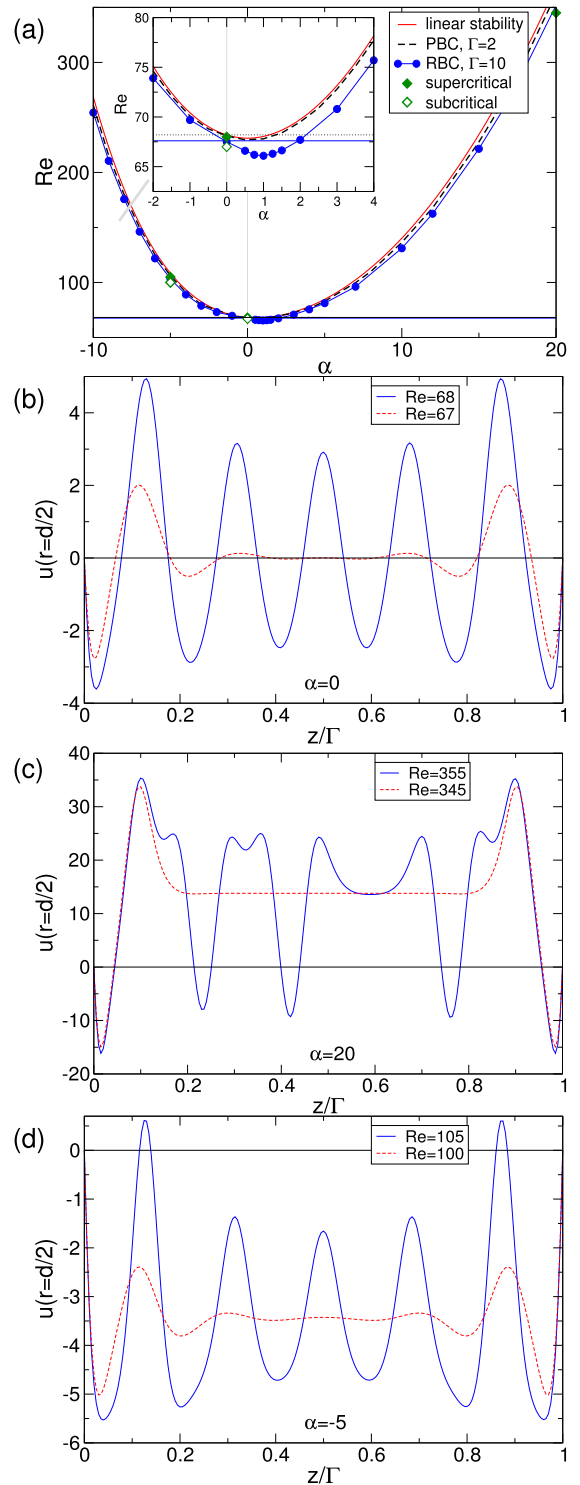


**Fig. 2.** Subcritical and supercritical flow states. (a) The transition boundary between subcritical and supercritical flow states (in absence of magnetic field,  $s_x = 0$ ) for periodic boundary conditions (PBC,  $\Gamma = 2$ ) corresponding to infinitely long cylinders and rigid boundary conditions (RBC,  $\Gamma = 10$ ) for a finite length system. The solid (red) curve shows the results of a linear stability analysis [45]. The horizontal line corresponds to the value for the critical Reynolds numbers  $Re_c$  with  $\alpha = 0$ . Open and filled diamonds in (a) indicate the parameters ( $Re$ ,  $\alpha$ ) for subcritical and supercritical flow states, for which radial velocity profiles  $u(r = d/2)$  at mid-gap are shown in (b) for  $\alpha = 0$ , (c)  $\alpha = 20$  (here the supercritical flow is given as a wavy vortices with a single dislocation [9]) and (d)  $\alpha = -5$ , respectively. The inset in (a) gives a close-up of the region for which  $\alpha$  has a destabilizing effect. See text for further description. The Figs. 2–4 and 7–9 have been generated by Xmgrace..

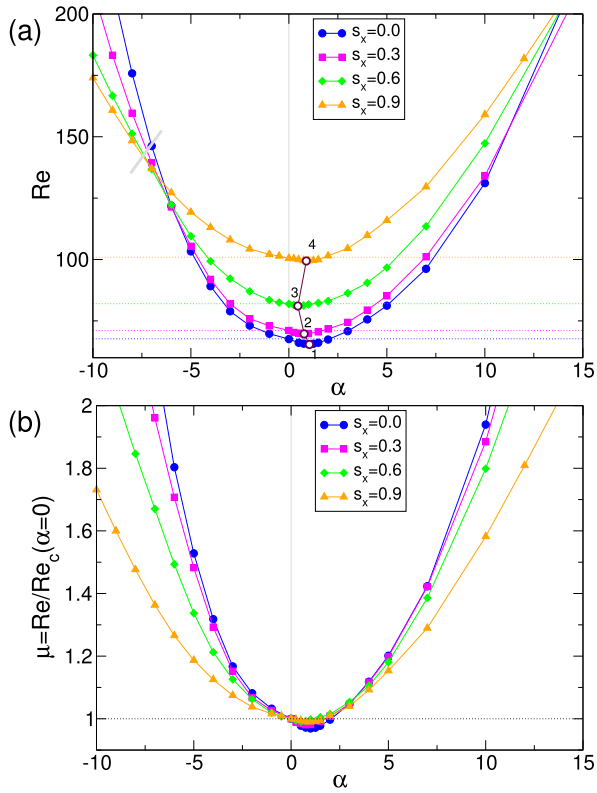


**Fig. 3.** Parameter space diagram ( $Re$ ,  $\alpha$ ) with varying  $s_x$ . Parameter space diagram for the transition boundary and supercritical flow states. Shown are (a) the ( $Re$ ,  $\alpha$ ) parameter space and (b) the normalized ( $\mu_{c,0}$ ,  $\alpha$ ) parameter space ( $\mu_{c,0} = Re/Re_c(\alpha = 0)$ ). Insets present close ups of the region, in which  $\alpha$  has destabilizing effect onto the flow structures. Points 1 to 4 indicate the parameters for maximal destabilization due to  $\alpha$ . The curve for  $s_x = 0.0$  is a replot of the one presented in Fig. 2.

endwalls for comparison and code verification. No-slip boundary conditions are used on the cylinders. In a cylindrical coordinate system ( $r$ ,  $\theta$ ,  $z$ ), the velocity field is  $\mathbf{u} = (u, v, w)$  and the corresponding vorticity field is  $\nabla \times \mathbf{u} = (\xi, \eta, \zeta)$ . The radius ratio of the cylinders,  $\beta = R_i/R_o$ , is kept fixed at 0.5. For stationary endwalls (RBC) the aspect ratio for axial height  $L$  is set to  $\Gamma = L/d = 10$ , while for PBC it is set to  $\Gamma = 2$ , where  $d = R_o - R_i$  is the gap between the cylinders.

A homogeneous magnetic transverse orientated magnetic field  $\mathbf{H}_{ext} = H_x \hat{e}_x$  (Fig. 1) is considered (with  $H_x$  being the field strength normal to the axis of the system). The length and time scales of the system are set by the gap width,  $d$ , and the diffusion time,  $d^2/\nu$ , respectively. The pressure in the fluid is normalized by  $\rho\nu^2/d^2$ , and the magnetic field  $\mathbf{H}$  and the magnetization  $\mathbf{M}$  can be conveniently normalized by the quantity  $\sqrt{\rho/\mu_0} \nu/d$ , where  $\mu_0$  is the permeability of free space. These considerations lead to the following set of non-dimensional hydrodynamical equations [18,39]:

$$(\partial_t + \mathbf{u} \cdot \nabla) \mathbf{u} - \nabla^2 \mathbf{u} + \nabla p = (\mathbf{M} \cdot \nabla) \mathbf{H} + \frac{1}{2} \nabla \times (\mathbf{M} \times \mathbf{H}), \quad (1)$$

$$\nabla \cdot \mathbf{u} = 0.$$

A radial through-flow is imposed at both the inner and outer permeable cylinders with radial Reynolds number

$$\alpha = u_i R_i / \nu,$$

with  $\alpha > 0$  for outflow and  $\alpha < 0$  for inflow. On the cylindrical surfaces, the dimensionless velocity fields are  $\mathbf{u}(r_i, \theta, z) = (\alpha(1/\beta - 1), Re_i, 0)$  and  $\mathbf{u}(r_o, \theta, z) = (\alpha(1 - \beta), 0, 0)$ , where  $u_i$  is the radial velocity at the non-dimensional inner cylinder radius,  $r_i = R_i/d$ , and is the radial velocity at the non-dimensional outer cylinder radius,  $r_o = R_o/d$ . The

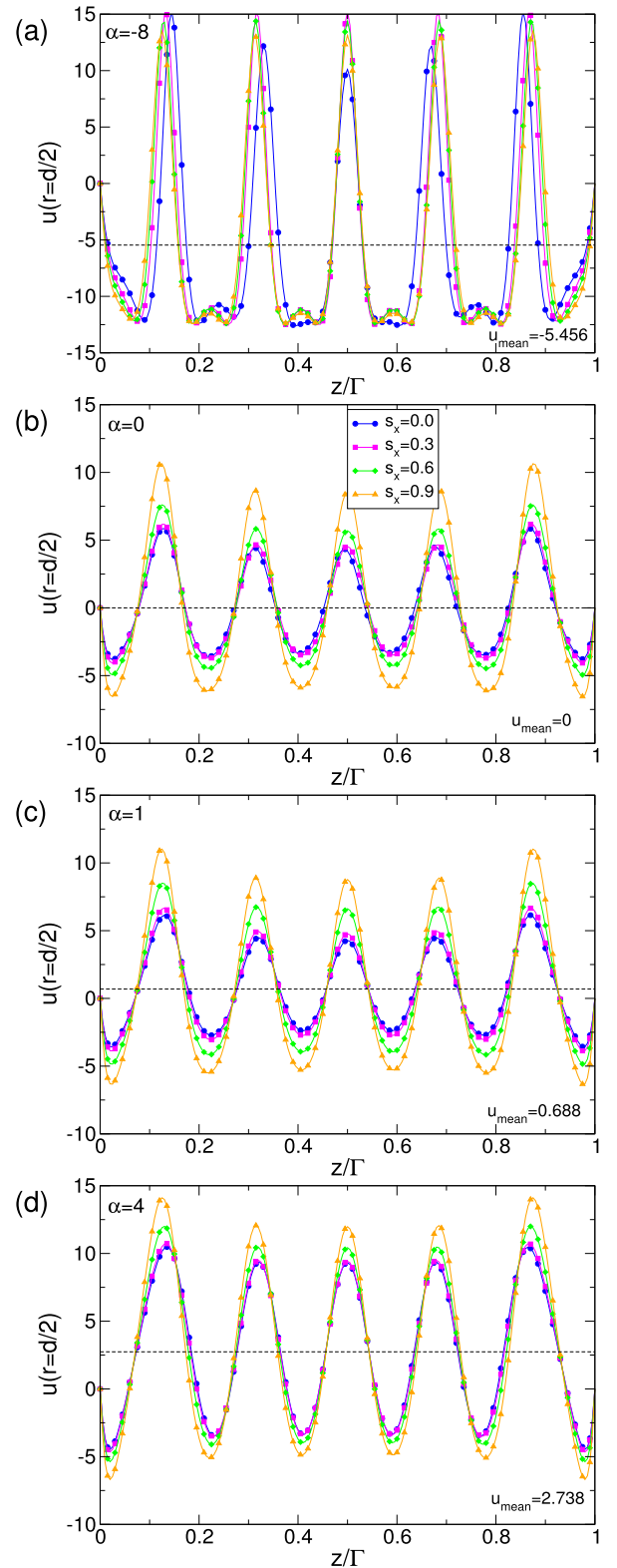
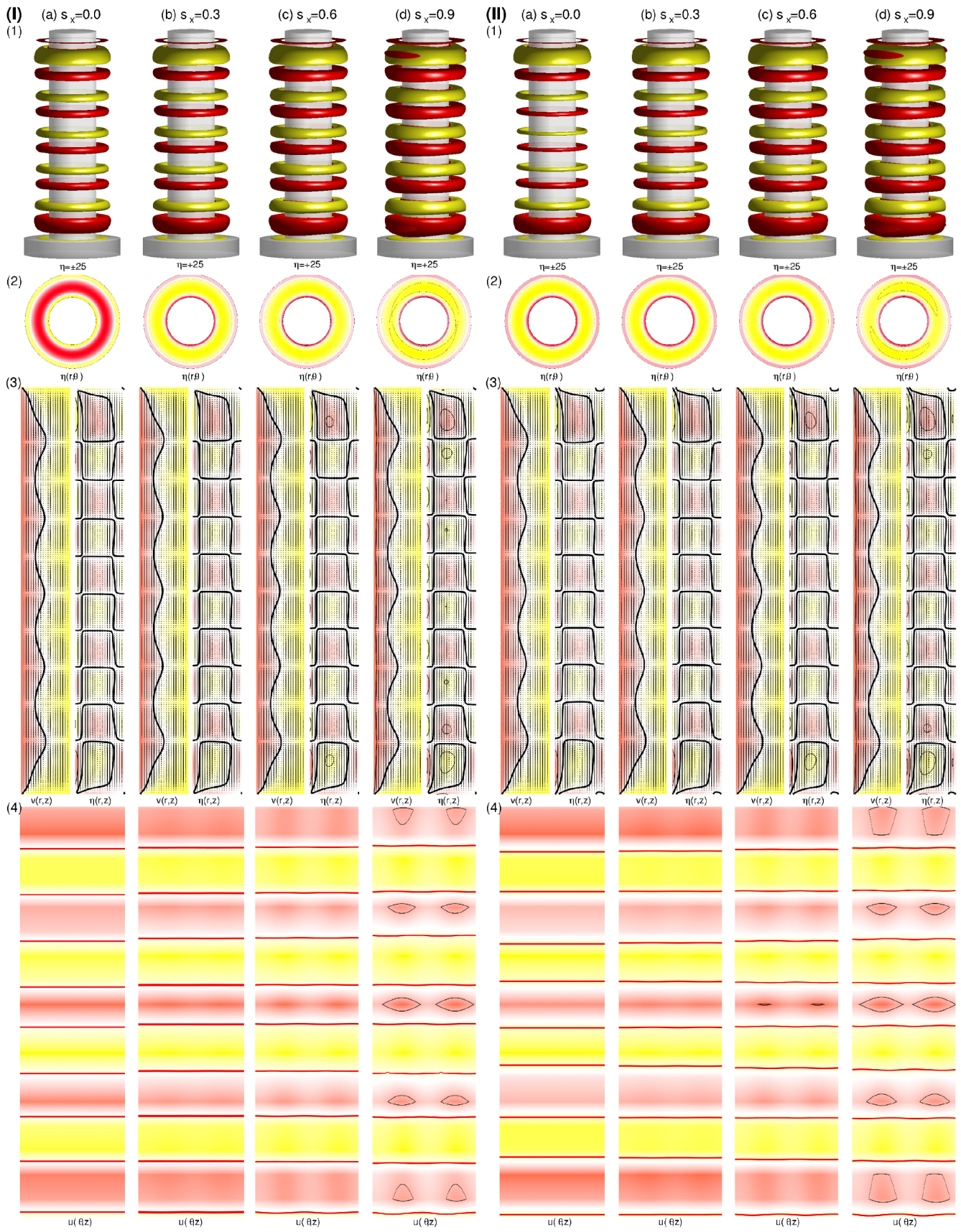


**Fig. 4.** Radial velocity profiles for flow states at different  $\alpha$ . Radial velocity profiles  $u(r = d/2)$  for  $\epsilon = Re(\alpha)/Re_c(\alpha) = 1.1$  (10% above the transition to supercritical flow states) at (a)  $\alpha = -8$ ; (b)  $\alpha = 0$ ; (c)  $\alpha = 1$ ; (d)  $\alpha = 4$ .

(inner) rotating Reynolds number is

$$Re_i = \omega_i R_i d / \nu.$$

Since the outer cylinder is at rest and only the inner cylinder rotates, we replace  $Re_i$  with  $Re$ .



(caption on next page)

**Fig. 5.** Visualization of different flow states for  $\alpha = 0$  and  $\alpha = 1$ . Visualization of the different 10% supercritical flow states,  $\epsilon = 1.1$ , at  $\alpha = 0$  ((I) left) and  $\alpha = 1$  ((II) right) and  $s_x$  as indicated. Shown are (1) isosurfaces of azimuthal vorticity  $\eta = \partial_z u - \partial_r w$  [red (dark gray) and yellow (light gray) colors correspond to positive and negative values, respectively]; (2) azimuthal vorticity  $\eta$  in the  $(r, \theta)$  plane at mid-height. (3) vector plots  $[u(r, z), w(r, z)]$  of the radial and axial velocity components (including (3.1) the azimuthal velocity  $v$  and (3.2) the azimuthal vorticity  $\eta$ ); (4) the radial velocity  $u(\theta, z)$  on an unrolled cylindrical surface in the annulus at mid-gap [red (yellow) color indicates in (out) flow]. Thick black lines in (3) corresponds to contours  $v/Re = 0.5$  (left) and into  $\eta = 0$  (right), respectively. Both Figs. 5 and 6 have been generated by MATLAB..

Eq. (1) is to be solved together with an equation that describes the magnetization of the ferrofluid. Using the approach of Niklas [13] and some further simplifications (see Appendix for details) leads to the following ferrohydrodynamical equations.

$$\begin{aligned} & (\partial_t + \mathbf{u} \cdot \nabla) \mathbf{u} - \nabla^2 \mathbf{u} + \nabla p_M \\ & = s_N^2 \left\{ \nabla^2 \mathbf{u} - \lambda_2 [\nabla \cdot (\mathbb{S}\mathbf{H})] - \mathbf{H} \times \left[ \frac{1}{2} \nabla \times (\nabla \times \mathbf{u} \times \mathbf{H}) - \mathbf{H} \times (\nabla^2 \mathbf{u}) \right. \right. \\ & \quad \left. \left. + \lambda_2 \nabla \times (\mathbb{S}\mathbf{H}) \right] \right\}, \end{aligned} \quad (2)$$

where  $\mathbb{S}$  is the symmetric component of the velocity gradient tensor [18,39], and  $\lambda_2$  is the material-dependent transport coefficient [25,39,40]. (In the present work, we set  $\lambda_2 = 0.8$ , based on experimental observations [40–43].) The effect of the magnetic field and the magnetic properties of the ferrofluid on the velocity field can be characterized by a single parameter, the magnetic field or the Niklas parameter [13], here  $s_N^2 = s_x^2$ , with

$$s_x^2 = \frac{2(2 + \chi)H_k c_N}{(2 + \chi)^2 - \chi^2 \eta^2}. \quad (3)$$

Here,  $\chi$  is the magnetic susceptibility of the ferrofluid, which can be approximated by Langevin's formula [44], and the Niklas coefficient  $c_N$  depends on the properties of the ferrofluid and magnetic field [13,25], as described in the Appendix. The numerical approach to solving the equations is outlined in the Appendix.

### 3. Results

#### 3.1. Parameter space and flow detection

In the absence of any magnetic field ( $s_x = 0$ ) or radial through-flow ( $\alpha = 0$ ), the basic flow state, CCF, becomes unstable against axisymmetric TVF at a critical Reynolds number of  $Re_c = 67.6$  for  $\Gamma = 10$  ( $Re_c = 68.1$  for PBC) for  $\beta = 0.5$  with no radial flow or magnetic field. Based on a linear analysis of infinitely long cylinders, the corresponding critical Reynolds number is  $Re_c = 68.19$  and critical wavenumber is  $k_c = 3.16$  [46]. Hence, the aspect ratios of  $\Gamma = 10$  for RBC and  $\Gamma = 2$  for PBC are reasonable choices given the similar axial wavenumber of  $k = \pi$ .

The stability thresholds for RBC, PBC, and a linear analysis [45] with radial flow, but without any applied magnetic field, are shown in Fig. 2(a). The results for the numerical code for PBC with an axial wavenumber of  $k = \pi$  match the linear stability analysis over the range  $-10 \leq \alpha \leq 20$ , thereby verifying the code. The system is stabilized for  $\alpha < 0$  as well as  $\alpha \gtrsim 1.9$  for RBC [ $\alpha \gtrsim 1.3$  for PBC and linear analysis] (see inset for detail), whereas it becomes slightly destabilized for  $0 < \alpha \lesssim 1.9$  [ $0 < \alpha \lesssim 1.3$ ]. The minimum in the stability curve, corresponding to  $Re/Re_c = 0.97$  for RBC [ $Re/Re_c = 0.99$  for PBC and linear analysis], occurs at  $\alpha = 1.05$  [ $\alpha = 0.65$  for PBC and linear analysis]. The shift of the stability threshold to a lower  $Re$  for the finite length system is related to the Ekman layers adjacent to the endwalls [47–53]. These subcritical structures trigger the centrifugal instability to grow at lower  $Re$ .

For the remainder of this paper we will restrict our investigation to RBC and focus on the influence of variation of an external applied magnetic field in a finite length system. For context, Fig. 2(c) and (d) shows examples of the radial velocity at the mid-gap as a function of the axial position for subcritical and supercritical flow states

(corresponding to diamond symbols in Fig. 2(a)) in the absence of a magnetic field for zero radial flow ( $\alpha = 0$ , Fig. 2(b)), radial outflow ( $\alpha = 20$ , Fig. 2(c)), and radial inflow ( $\alpha = -5$ , Fig. 2(d)). The horizontal lines in Fig. 2(a) correspond to the values for the critical Reynolds numbers  $Re_c$  with  $\alpha = 0$  for PBC and linear stability (upper horizontal line) and RBC (lower horizontal line). The short gray line in (a) as well in Fig. 3 at  $\alpha \approx -7.5$  indicate the change in subcritical flow structures from TVF ( $\alpha \lesssim -7.5$ ) to wTVF ( $\alpha \gtrsim -7.5$ ) (see also [9]). Note that  $k_c = 3.16$  for RBC is slightly different than  $k_c = \pi$ , used either for PBC and linear analysis. For all cases, the subcritical flow states (dashed lines) display vortical motion (peaks in radial velocities) due to Ekman endwall pumping that decrease rapidly moving away from endwall. The radial velocity has a flat, nearly constant profile in the middle portion of the length of the annulus with a value that depends on the applied radial through-flow  $\alpha$ : zero for no radial flow, above zero for positive  $\alpha$ , and below zero for negative  $\alpha$ . On the other hand, for supercritical flow states the peaks and valleys in profile of the radial velocities represent outflow and inflow regions of pairs of vortical structures. The extrema are similar in amplitude except near the endwalls where the Ekman pumping amplifies their magnitude. The profiles in Fig. 2(b and d) have relatively uniform peaks corresponding to a supercritical flow state of TVF. On the other hand, Fig. 2(c) for radial outflow has a profile characteristic of wavy vortex flow, wTVF, plus a dislocation, as previously reported by Serre et al. [9]. As will be shown shortly, the presence of a magnetic field changes the spatio-temporal structure of such dislocations as well as the range of parameter space over which they exist.

#### 3.2. Bifurcation and stability thresholds

A transverse magnetic field influences the stability system. We restrict this study to three magnetic field strengths:  $s_x = 0.3$ ,  $s_x = 0.6$  and  $s_x = 0.9$ , which are all within range of experimental studies [54,55]. Fig. 3 illustrates the stability thresholds between subcritical and supercritical flow states as the radial through-flow is varied for different magnetic field strengths including  $s_x = 0.0$ , which was shown in Fig. 2(a)). In absence of radial flow, corresponding to  $\alpha = 0$ , the well known stabilizing effect of an external magnetic field is obvious [13,14,16–18,23,24], as the stability thresholds are shifted upward to larger  $Re$  in Fig. 3(a) (horizontal dotted lines indicate the critical thresholds for  $\alpha = 0$ ). Likewise, the entire stability curve shifts upward with increasing  $s_x$ . However, the behavior with the radial flow,  $\alpha$ , is similar, regardless of the magnetic field strength. That is, radial inflow,  $\alpha < 0$ , stabilizes the transition, small outflow corresponding to small positive  $\alpha$  destabilizes the transition slightly, and sufficiently large positive  $\alpha$  stabilizes the transition.

Interestingly, the parameter region in which the destabilization occurs due to a small radial outflow does not change monotonically with the magnetic field strength. In the absence of a magnetic field,  $s_x = 0.0$ , the destabilized region is  $0 < \alpha \lesssim 2.05$ . The region shrinks for  $s_x = 0.3$  to  $0 < \alpha \lesssim 1.75$  and then shrinks further for  $s_x = 0.6$  to  $0 < \alpha \lesssim 1.2$  before it increases again for  $s_x = 0.9$  to  $0 < \alpha \lesssim 1.8$ . The value for  $\alpha$  that has the maximum destabilizing effect,  $\alpha_c$ , also depends non-monotonically on the applied magnetic field, as is evident from the points labeled 1–4 in Fig. 3(a). Furthermore, the degree of destabilization changes with the applied magnetic field, as is evident in Fig. 3(b) where the normalized critical Reynolds number,  $\mu_{c,0} = Re/Re(\alpha = 0)$ , is plotted as a function of  $\alpha$ . Initially,  $\mu_{c,0} = 0.968$  at  $\alpha \approx 1.05$  without a

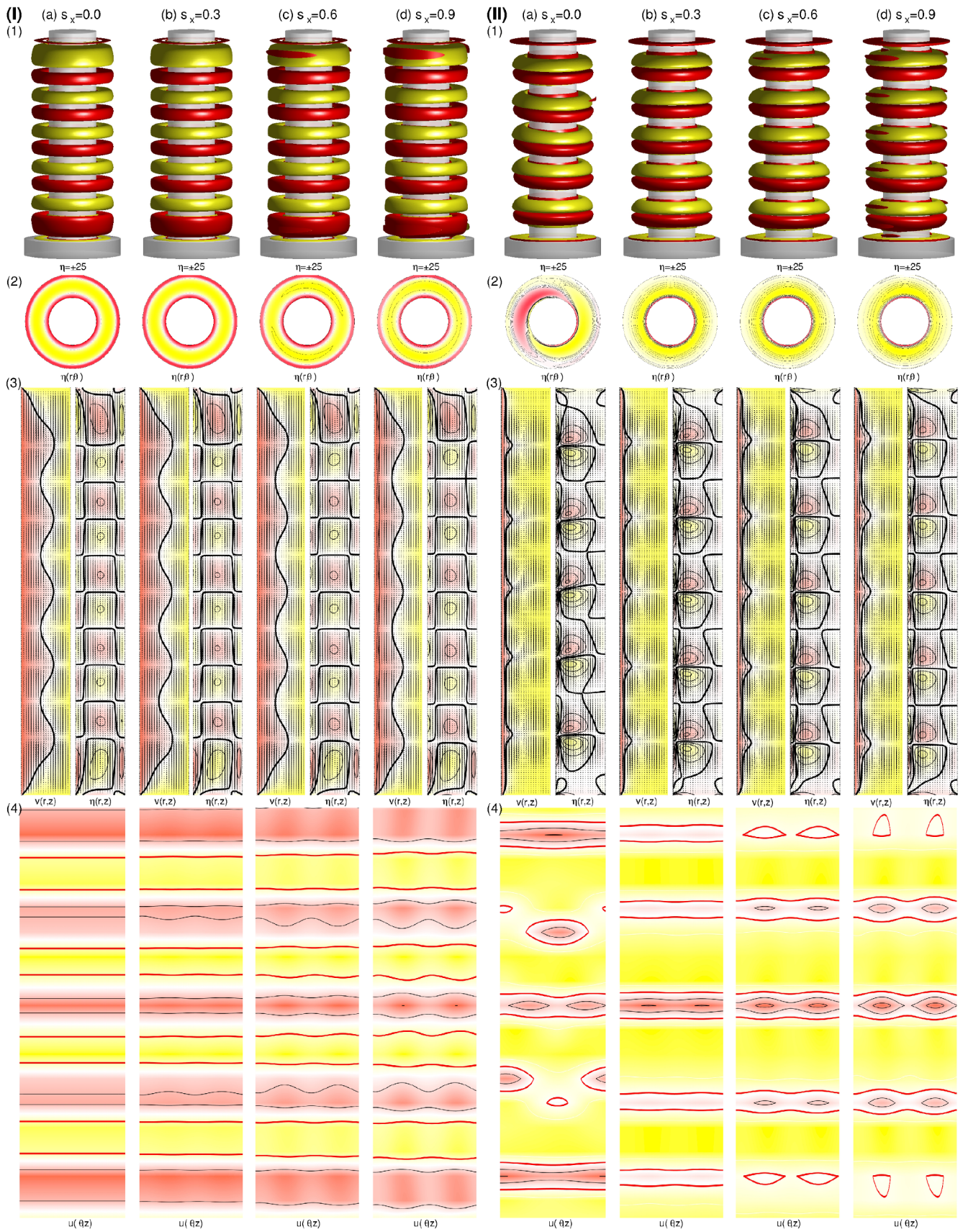


Fig. 6. Visualization of the different flow states for  $\alpha = 4$  and  $\alpha = -8$ . As Fig. 5 but for  $\alpha = 4$  ((I) left) and  $\alpha = -8$  ((II) right), respectively.

magnetic field,  $s_x = 0.0$ . It increases to  $\mu_{c,0} = 0.98$  at  $\alpha \approx 0.75$  for  $s_x = 0.3$  to  $\mu_{c,0} = 0.992$  at  $\alpha \approx 0.51$  at  $s_x = 0.6$  before it increases again to  $\mu_{c,0} = 0.987$  at  $\alpha \approx 0.95$  for  $s_x = 0.9$ .

Unlike the destabilizing effect for small positive  $\alpha$ , which remains essentially unchanged with an applied magnetic field, the stabilizing effect depends strongly on  $s_x$ . Increasing the magnetic field strength  $s_x$  changes the curvature of the bifurcation thresholds to become less convex and wider (Fig. 3(b)). This means that for sufficiently negative  $\alpha$ , a stronger magnetic field decreases the stability, while increasing the magnetic field stabilizes the flow for  $\alpha \gtrsim -6$  (Fig. 3(a)).

### 3.3. Flow structures – spatial dynamics

Fig. 4 presents the radial velocity profiles  $u(r = d/2)$  for selected radial through-flows  $\alpha = -8, 0, 1, 4$  and different field strengths  $s_x = 0.0, 0.3, 0.6, 0.9$ , as indicated. The velocity is shown for a value of  $Re$  that is 10% above the transition to supercritical flow, designated as  $\epsilon = Re(\alpha)/Re_c(\alpha) = 1.1$ . For any given value of  $\alpha$  the imposition of a magnetic field affects the amplitude of the mid-gap radial velocity, but otherwise makes little difference. The magnetic field increases both the inflow (negative  $u$ ) and outflow (positive  $u$ ) magnitudes, though the increase is larger for the outflow. The case of  $\alpha = -8$  is a bit different for the radial inflow than those with  $\alpha \geq 0$ . This is a result of the vortical structure becoming wavy, evident as the flattened inflow radial velocity.

Further insight into the physics leading to the stabilizing and destabilizing effects of radial flow combined with a transverse magnetic field can be obtained from Figs. 5 and 6, which visualize the different flow states for fixed  $\alpha = -8, 0, 1, 4$  and change of magnetic field strength  $s_x$ . The top row of both figures shows isosurfaces of the azimuthal vorticity,  $\eta = \partial_z u - \partial_r w$ , where red (dark gray) and yellow (light gray) colors correspond to positive and negative values, respectively. For all  $\alpha$  the contours expand at (constant value  $\eta = \pm 25$ ) as  $s_x$  increases indicating that the entire vortex structure becomes stronger. However for  $s_x = 0$  the flow remains purely axisymmetric (Fig. 5(a)), the classical TVF. Increasing  $s_x$  forces the well known 2-fold symmetry due to a transverse magnetic field [25,17] (Figs. 5 and 6(2)(4)). Regarding the 50% contour line of the azimuthal velocity  $v/Re = 0.50$  (Fig. 5(3.1)) one sees an increase in modulation amplitude, minima and maxima increase, respectively, similar to the radial velocity profiles presented in Fig. 4. Same observations also hold for Fig. 6 with the main difference, that the 50% contour line of the azimuthal velocity  $v/Re = 0.50$  is moving outwards for larger and inwards for smaller  $\alpha$ . Here it is worth to mention that Fig. 6 presents a wavy TVF state (wTVF), which already has finite  $m = 1$  mode contribution (Fig. 6(2), (4)). However, the Figs. 5 and 6 can't explain the change in stabilizing effect due to interaction of transverse field and radial flow, i.e. the modification in curvature in Fig. 3, it's more flat.

In order to get insight into the physics leading to the modification in the bifurcation/stability thresholds, we focus on the azimuthal flow, which is the dominant flow in the annulus (at least for the conditions investigated here). Therefore we consider the 50% contour line of the dimensionless azimuthal velocity  $v/Re = 0.50$ , but for two different positions in the bulk,  $\theta = 0$  (aligned with the magnetic field) and  $\theta = \pi/2$  (perpendicular to the magnetic field) and their variation for different radial flows  $\alpha$  at 10% supercritical flow states  $Re/Re_c = 1.1$  as illustrated in Fig. 7 (vertical gray line at  $r = 1.5$  indicates the mid-gap of the bulk). Independent of an applied magnetic field, the contours are shifted into the direction of the radial flow  $\alpha$ ; for negative  $\alpha$  inwards and for positive  $\alpha$  outwards, respectively (i.e. in Fig. 7 from left to right with increasing  $\alpha$ ). In addition to shifting outward, the bulges in the contours increase with  $\alpha$ . These contours grow in radial extent with increasing radial outflow as the imposed radial flow enhances the vortical outflow. Likewise, the inward bulges in the contour grow for radial inflow, indicating an enhancement of the vortical inflow.

However, a significant point we neglected so far is the fact that the

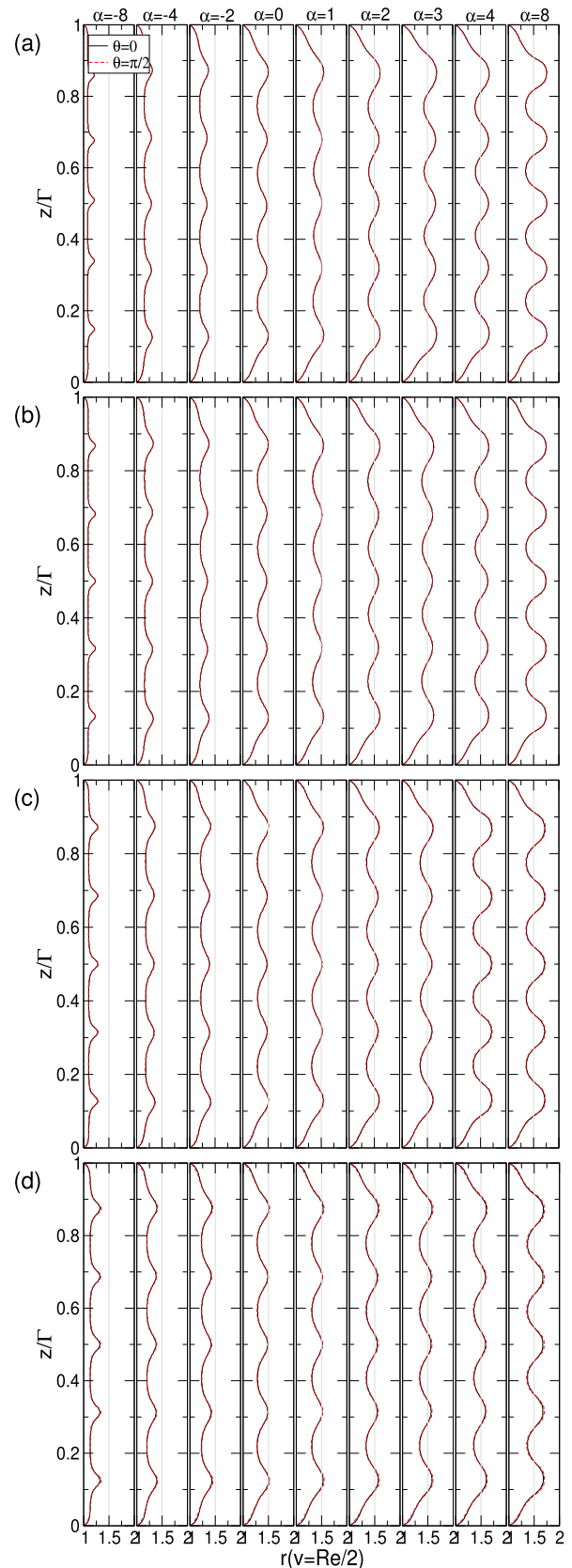
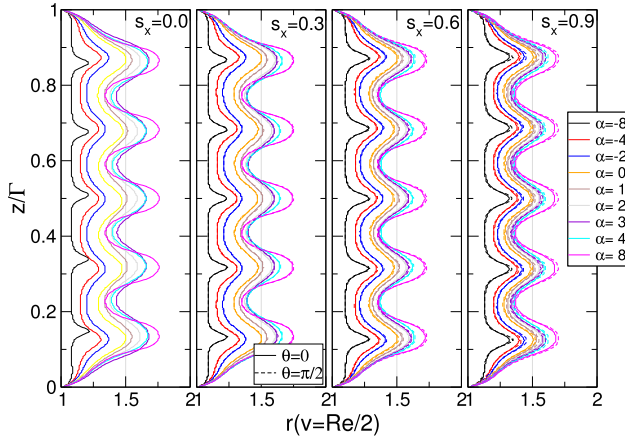


Fig. 7. Azimuthal velocity contour profiles in bulk gap with variation of  $\alpha$  for flow states at different  $s_x$ . Azimuthal velocity contour profiles for  $v = Re/2$  in the bulk gap  $([1, 2])$  at  $\alpha \in [-8, -4, -2, 0, 1, 2, 3, 4, 8]$  (from left to right) as indicated for (a)  $s_x = 0.0$ ; (b)  $s_x = 0.3$ ; (c)  $s_x = 0.6$ ; (d)  $s_x = 0.9$  (see also Figs. 5 and 6). Note the vertical gray lines at  $r = 1.5$  indicates the mid-gap of the bulk.



**Fig. 8.** Velocity contour profiles with variation of  $\alpha$  for flow states at different  $s_x$ . Azimuthal velocity contour profiles for  $v = Re/2$  at  $\alpha$  and  $s_x$  as indicated (see also Fig. 7). Note the vertical line at  $r = 1.5$  indicates the (radial) center of the bulk. Solid lines indicate contours at  $\theta = 0$  (field aligned) and dashed lines indicate contours at  $\theta = \pi/2$  (perpendicular to the field.), respectively.

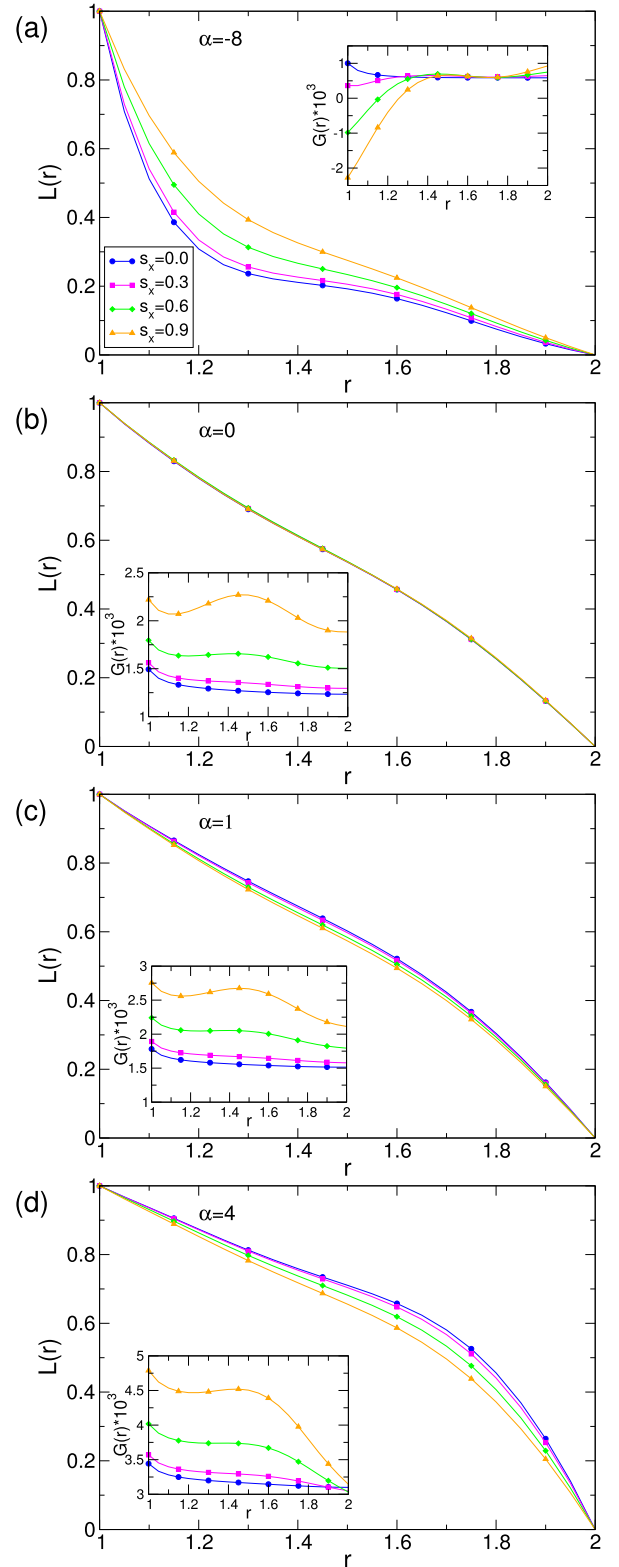
bulges in the contours for  $\theta = 0$  (along the applied field direction, solid black curves in Fig. 7) and  $\theta = \pi/2$  (perpendicular to the applied field direction, dashed red curves in Fig. 7) are different as soon a finite magnetic field ( $s_x \neq 0$ ) is present. More important, the differences detected in the contours increases with increasing field strength  $s_x$  and such is largest for  $s_x = 0.9$  (Fig. 7(d)). However, in addition the difference also increases with  $\alpha$  at any constant value  $s_x$  (from left to right in Fig. 7); smallest for  $\alpha = -8$  and largest for  $\alpha = 8$ . In any case the variation of amplitude (between min and max) is larger for  $\theta = \pi/2$ .

Fig. 8 gives another perspective of the change in contours with increasing through flow  $\alpha$  at different magnetic field strength  $s_x$ . It clearly indicates the outward move of contours ( $v = Re/2$ ) and growing bulges with increasing radial flow  $\alpha$ . The differences for  $\theta = 0$  and  $\theta = \pi/2$  enlarges with  $s_x$  and in parallel becomes more pronounced with increasing  $\alpha$ . This variation in profiles for  $\theta = 0$  (along the applied magnetic field) and  $\theta = \pi/2$  (perpendicular to the applied magnetic field) is the reason for the change in shape and expansion of the bifurcation threshold with  $s_x$  (Fig. 3). The larger  $s_x$ , the larger the differences between both azimuthal positions (Figs. 7 and 8). Due to this spatial variation, for a given radial flow, the system can be at the same time locally subcritical and locally supercritical, respectively. This partial sub- and supercritical flow regimes within the bulk delays the grow of any fully developed supercritical vortex structure. Finally the overall result is a weaker stabilizing effect with  $\alpha$ , the curves in  $(\alpha, Re)$  parameter space (Fig. 3) become wider.

### 3.4. Angular momentum transport

To further characterize the modification of the stability thresholds due to interaction of radial flow and magnetic field, we examine the behavior of the angular momentum and torque for a variety of flow conditions. Fig. 9 shows the mean (axially and azimuthally averaged) angular momentum  $L(r) = r\langle v(r) \rangle_{\theta,z}/Re$ , as a function of the radius  $r$  for different  $\alpha$  and  $s_x$ . As before all flow states are 10% supercritical,  $\epsilon = 1.1$ , as already used before.

All curves show one main characteristic. In general, the angular momentum curves follow a monotonically varying trend. The profiles indicate typical behavior in that positive angular momentum decreases outward from the rotating inner cylinder to the stationary outer cylinder. Depending on both parameters, radial flow  $\alpha$  and field strength  $s_x$ , one observes a more constant region (plateau-like) within the bulk. In absence of radial flow  $\alpha = 0$  (Fig. 9(b)) the angular momentum decreases with almost constant slope from inner towards the outer



**Fig. 9.** Variation in angular momentum and torque for flow states at different  $\alpha$ . Angular momentum  $L(r) = r\langle v(r) \rangle_{\theta,z}/Re$  versus the radius  $r$  for flow states at (a)  $\alpha = -8$ ; (b)  $\alpha = 0$ ; (c)  $\alpha = 1$ ; (d)  $\alpha = 4$ . The insets show corresponding variation of the dimensionless torque  $G = \nu J^\omega$  (see text for details) versus the radius  $r$ . All flow states are 10% supercritical and correspond to flow states presented in Figs. 5 and 6.

cylinder virtually unaffected from the strength  $s_x$  of an applied magnetic field. Here all curves fall on top of each others. Increasing  $\alpha$  towards more positive values (Fig. 9(c and d)) result in the formation of a more and more ‘belly-like’ shape, which grows outwards and result in steeper slopes of the curves near the outer cylinder. On the other hand radial inflow,  $\alpha < 0$ , (Fig. 9(a)) results in steeper slopes near the inner cylinder with the profiles flatten slightly in the middle of the annular gap to form a horizontal plateau. Further, we focus closer on the effect onto the curves due to variation in  $s_x$ . For positive  $\alpha$  an increase in  $s_x$  results in a minimizing of the ‘belly’ structure evolving for larger  $\alpha$  (Fig. 9(c, d)); the curves move downwards. Interestingly the effect of increasing  $s_x$  for negative radial flow,  $-\alpha$ , is just opposite. The internal plateau shape structure in Fig. 9(a) becomes diminished as the curves move upwards. Thus, larger  $s_x$  ‘simplify’ the curves with respect to the angular momentum.

The insets in Fig. 9 show the corresponding variation of the dimensionless torque  $G = \nu J^\omega$  within the annulus. In calculating the torque we used the fact that for a flow between infinite cylinders the transverse current of the azimuthal motion,  $J^\omega = r^3 [\langle u\omega \rangle_{A,t} - \nu \langle \partial_r \omega \rangle_{A,t}]$  (with  $\langle \dots \rangle_A \equiv \frac{rd\theta dz}{2\pi r l}$ ), is a conserved quantity [56]. For positive and zero  $\alpha$  and increasing  $s_x$  the torque profile changes from a flat, almost constant mid-gap region towards a parabola, belly-like shape at mid-gap (insets in Fig. 9(b–d)). As with the angular momentum, the profiles of  $G(r)$  show a generally monotonically varying trend as  $s_x$  increases with very little difference. However, for radial inflow (Fig. 9(a)), the situation is more complex. As one sees in the inset of Fig. 9, the variation in the curve due to increasing  $s_x$  are not monotonic anymore. With respect to  $G(r)$  decreases near the inner cylinder. For larger  $s_x$  it decreases, while for larger  $\alpha$  it increases instead. However, here in any case an almost horizontal plateau within the profiles remain preserved.

#### 4. Summary

The present studies provide new insight into the connection and interaction between radial through-flow and an external applied homogeneous transverse magnetic and therefrom resulting consequences for instabilities. Aside the stabilizing effect of the magnetic field, the effect of radial flow is qualitative similar for different magnetic field strengths. For any radial inflow and ‘sufficient (fairly)’ large radial outflow the vortices in the flow structures become suppressed, which leads to a stabilizing of the basic state, compared to the situation without any radial flow, i.e. the bifurcation thresholds are moved upwards to larger critical values. On the other hand a moderate radial outflow has the opposite effect, resulting in destabilization of the basic state. The bifurcation thresholds are moved towards smaller critical values. This is qualitative analog to the situation in absence of any applied magnetic field.

However, quantitative there are various significant differences if a magnetic field is present. First to mention, either the parameter region for which the radial flow has stabilizing effect, as well as the amount of

destabilization depend crucially on the strength of the applied magnetic field. No direct and simple correlation can be extracted between field strength and resulting (de-) stabilizing effect. For small and moderate field strength the region shrinks, while for larger field strength it expands again, so that there is no monotonic behavior. Second and even more interesting is the variation/modulation in curvature, speaking in  $(\alpha, Re)$  parameter space due to variation of the magnetic field. The larger the magnetic field strength  $s_x$ , the less pronounced/influence becomes the effect due to radial flow  $\alpha$ . Thus the curves  $(\alpha, Re)$  parameter space become more convex with less curvature, i.e. more flat. Quantitatively the relative stabilization effect of  $\alpha$  becomes weakened with increasing  $s_x$ . The reason for this modification in the stability thresholds is found to be originated/forced by the symmetry breaking nature of a transverse magnetic field itself. In general the vortices themselves together with the azimuthal velocity iso-contours are shifted in the direction of the applied radial flow. Thus for radial inflow the vortex center move inwards while for radial outflow they move outwards, respectively. However, the symmetry breaking nature of the transverse magnetic field results in differences in the shift between both directions along the applied magnetic field and perpendicular to the field. In particular the modulation amplitude in the iso-contours perpendicular to the field becomes stronger/increased. As a result the flow can be locally stabilized with different strength, so that the overall stabilization is weaker relative to the situation without any applied field. As the differences in modifications in the flow aligned with the field and perpendicular to it increase with increasing field strength  $s_x$ , the overall stabilization becomes also weaker, the curves move to lower critical values. Thus one could argue the transverse field results in a local pinning, which reduces the effect of radial flow.

As this work presents the first investigation of the effects of  $\alpha$  and  $s_x$ , we only considered azimuthal, toroidally closed,  $m = 0$  mode dominated flow structures. Further interesting future work will be the investigation of the effect radial through flow and magnetic field have on helical spiral structures. As typically such helical solutions already incorporate higher spatio-temporal dynamics, one can expect an even stronger influence of radial flow and magnetic field, either in internal dynamics of the flow as well as stability thresholds. Moreover an expansion to study the combination of ferrofluid flow under either radial and additional axial through flow could be quite interesting.

#### Declaration of Competing Interest

The authors declare that they have no known competing financial interests or personal relationships that could have appeared to influence the work reported in this paper.

#### Acknowledgments

S.A. is a Serra Hünter Fellow. This work was supported by the Spanish Government grant FIS2017-85794-P.

#### Appendix A. Appendix

##### A.1. Ferrohydrodynamical equation

Eq. (1) is to be solved together with an equation that describes the magnetization of the ferrofluid. Using the equilibrium magnetization of an unperturbed state in which the homogeneously magnetized ferrofluid is at rest and the mean magnetic moment is orientated in the direction of the magnetic field, we have  $\mathbf{M}^{\text{eq}} = \chi \mathbf{H}$ . The magnetic susceptibility  $\chi$  of the ferrofluid can be approximated by the Langevin’s formula [44], where we set the initial value of  $\chi$  to be 0.9 and use a linear magnetization law. The ferrofluid studied corresponds to APG933 [54]. We consider the near equilibrium approximations of Niklas [13,23] with a small value of  $\|\mathbf{M} - \mathbf{M}^{\text{eq}}\|$  and small magnetic relaxation time  $\tau: |\nabla \times \mathbf{u}| \tau \ll 1$ . Using these approximations, one can obtain [18] the following magnetization equation:

$$\mathbf{M} - \mathbf{M}^{\text{eq}} = c_N^2 \left( \frac{1}{2} \nabla \times \mathbf{u} \times \mathbf{H} + \lambda_2 \mathbf{S} \mathbf{H} \right), \quad (4)$$

where

$$c_N^2 = \tau / (1/\chi + \tau\mu_0 H^2 / 6\mu\Phi) \quad (5)$$

is the Niklas coefficient [13],  $\mu$  is the dynamic viscosity,  $\Phi$  is the volume fraction of the magnetic material,  $\mathbb{S}$  is the symmetric component of the velocity gradient tensor [39,18], and  $\lambda_2$  is the *material-dependent transport coefficient* [25,39,40], here fixed to 0.8 [40]. Using Eq. (4), we eliminate the magnetization from Eq. (1) to arrive at the following *ferrohydrodynamical equations* [39,18]:

$$\begin{aligned} & (\partial_t + \mathbf{u} \cdot \nabla) \mathbf{u} - \nabla^2 \mathbf{u} + \nabla p_M \\ &= -\frac{s_N^2}{2} [\mathbf{H} \nabla \cdot (\mathbf{F} + \lambda_2 \mathbb{S} \mathbf{H}) + \mathbf{H} \times \nabla \times (\mathbf{F} + \lambda_2 \mathbb{S} \mathbf{H})], \end{aligned} \quad (6)$$

where  $\mathbf{F} = (\nabla \times \mathbf{u}/2) \times \mathbf{H}$ ,  $p_M$  is the dynamic pressure incorporating all magnetic terms that can be expressed as gradients, and  $s_N$  is the *Niklas parameter* [Eq. (3)]. To the leading order, the internal magnetic field in the ferrofluid can be approximated by the externally imposed field [24], which is reasonable for obtaining the dynamical solutions of the magnetically driven fluid motion. Eq. (6) can then be simplified as

$$(\partial_t + \mathbf{u} \cdot \nabla) \mathbf{u} - \nabla^2 \mathbf{u} + \nabla p_M = s_N^2 \left\{ \nabla^2 \mathbf{u} - \lambda_2 [\nabla \cdot (\mathbb{S} \mathbf{H})] - \mathbf{H} \times \left[ \frac{1}{2} \nabla \times (\nabla \times \mathbf{u} \times \mathbf{H}) - \mathbf{H} \times (\nabla^2 \mathbf{u}) + \lambda_2 \nabla \times (\mathbb{S} \mathbf{H}) \right] \right\}, \quad (7)$$

as already presented in Eq. (2).

## A.2. Numerical methods

The ferrohydrodynamical equations of motion Eq. (6) are solved [25,24,18] by combining a standard, second-order finite-difference scheme in  $(r, z)$  with a Fourier spectral decomposition in  $\theta$  and (explicit) time splitting. The variables can be expressed as

$$f(r, \theta, z, t) = \sum_{m=-m_{\max}}^{m_{\max}} f_m(r, z, t) e^{im\theta}, \quad (8)$$

where  $f$  denotes one of the variables  $\{u, v, w, p\}$ . For the parameter regimes considered, the choice  $m_{\max} = 16$  provides adequate accuracy. We use a uniform grid with spacing  $\delta r = \delta z = 0.02$  and time steps  $\delta t < 1/3800$ . For diagnostic purposes, we also evaluate the complex mode amplitudes  $f_{m,n}(r, t)$  obtained from a Fourier decomposition in the axial direction:

$$f_m(r, z, t) = \sum_n f_{m,n}(r, t) e^{inkz}, \quad (9)$$

where  $k = 2\pi d/\lambda$  is the axial wavenumber.

Note that for a ferrofluid in presence of a *transverse* magnetic field ( $s_x \neq 0$ ), the symmetries present in classical TCS (arbitrary rotations about the axis and the reflections about axial mid-height) are broken and the flow is *inherently three-dimensional* for any combination of non-zero values of the parameters  $Re$  and  $s_x$  [14,17,18,24].

## Appendix B. Supplementary data

Supplementary data associated with this article can be found, in the online version, at <https://doi.org/10.1016/j.jmmm.2019.166363>.

## References

- [1] G.I. Taylor, Stability of a viscous liquid contained between two rotating cylinders, *Philos. Trans. R. Soc. London A* 223 (1923) 289.
- [2] R.C. DiPrima, H.L. Swinney, Instabilities and transition in flow between concentric rotating cylinders, in: H.L. Swinney, J.G. Gollub (Eds.), *Hydrodynamic Instabilities and the Transition to Turbulence*, number 45 in *Topics in Applied Physics*, Springer, Berlin, 1985.
- [3] T.S. Chang, W.K. Sartory, Hydromagnetic stability of dissipative flow between rotating permeable cylinders, *J. Fluid Mech.* 27 (1967) 65.
- [4] T.S. Chang, W.K. Sartory, Hydromagnetic stability of dissipative flow between rotating permeable cylinders. Part 2. Oscillatory critical modes and asymptotic results, *J. Fluid Mech.* 36 (1969) 193.
- [5] S.K. Bahl, Stability of viscous flow between two concentric rotating porous cylinders, *Def. Sci. J.* 20 (1970) 89.
- [6] K. Min, R.M. Lueptow, Hydrodynamic stability of viscous flow between rotating porous cylinders with radial flow, *Phys. Fluids* 6 (1994) 144.
- [7] E.C. Johnson, R.M. Lueptow, Hydrodynamic stability of flow between rotating porous cylinders with radial and axial flow, *Phys. Fluids* 9 (1997) 3687.
- [8] K. Bühler, *Ordered and Turbulent Patterns in Taylor-Couette Flow*, Plenum, New York, 1992.
- [9] E. Serre, M.A. Sprague, R.M. Lueptow, Stability of Taylor-Couette flow in a finite-length cavity with radial throughflow, *PoF* 20 (2008) 034106.
- [10] R.E. Rosensweig, *Ferrohydrodynamics*, Cambridge University Press, Cambridge, 1985.
- [11] J.P. McTague, Magnetoviscosity of magnetic colloids, *J. Chem. Phys.* 51 (1969) 133.
- [12] M.I. Shliomis, Effective viscosity of magnetic suspensions, *Sov. Phys. JETP* 34 (1972) 1291.
- [13] M. Niklas, Influence of magnetic fields on Taylor vortex formation in magnetic fluids, *Z. Phys. B* 68 (1987) 493.
- [14] S. Altmeyer, C. Hoffmann, A.L.M. Lücke, Influence of homogeneous magnetic fields on the flow of a ferrofluid in the Taylor-Couette system, *Phys. Rev. E* 82 (2010) 016321.
- [15] J. Linke, S. Odenbach, Anisotropy of the magnetoviscous effect in a cobalt ferrofluid with strong interparticle interaction, *J. Magn. Magn. Mater.* 396 (2015) 85.
- [16] M. Reindl, S. Odenbach, Influence of a homogeneous axial magnetic field on Taylor-Couette flow of ferrofluids with low particle-particle interaction, *Expts. Fluids* 50 (2011) 375.
- [17] M. Reindl, S. Odenbach, Effect of axial and transverse magnetic fields on the flow behavior of ferrofluids featuring different levels of interparticle interaction, *Phys. Fluids* 23 (2011) 093102.
- [18] S. Altmeyer, J. Lopez, Y. Do, Effect of elongational flow on ferrofluids under a magnetic field, *Phys. Rev. E* 88 (2013) 013003.
- [19] P. Chossat, G. Iooss, *The Couette-Taylor Problem*, Springer, Berlin, 1994.
- [20] C.A. Jones, The transition to wavy Taylor vortices, *J. Fluid Mech.* 175 (1985) 135.
- [21] C.D. Andereck, S.S. Liu, H.L. Swinney, Flow regimes in a circular Couette system with independently rotating cylinders, *J. Fluid Mech.* 164 (1986) 155.
- [22] M. Golubitsky, W.F. Langford, Pattern formation and bistability in flow between counterrotating cylinders, *Physica D* 32 (1988) 362.
- [23] M. Niklas, H. Müller-Krumbhaar, M. Lücke, Taylor-vortex flow of ferrofluids in the presence of general magnetic fields, *J. Magn. Magn. Mater.* 81 (1989) 29.
- [24] S. Altmeyer, J. Lopez, Y. Do, Influence of an inhomogeneous internal magnetic field on the flow dynamics of ferrofluid between differentially rotating cylinders, *Phys. Rev. E* 85 (2012) 066314.
- [25] S. Altmeyer, C. Hoffmann, A. Leschhorn, M. Lücke, Influence of homogeneous magnetic fields on the flow of a ferrofluid in the Taylor-Couette system, *Phys. Rev. E* 82 (2010) 016321.
- [26] S. Lee, R.M. Lueptow, Rotating membrane filtration and rotating reverse osmosis, *J. Chem. Eng. Jpn.* 37 (2004) 471.
- [27] R.M. Lueptow, A. Hajiloo, Flow in a rotating membrane plasma separator, *Trans. Am. Soc. Artif. Intern. Organs* 41 (1995) 182.
- [28] K. Ohashi, K. Tashiro, F. Kushiya, T. Matsumoto, S. Yoshida, M. Endo, T. Horio, K. Ozawa, K. Sakai, Rotation-induced Taylor vortex enhances filtrate flux in plasma separation, *Trans. Am. Soc. Artif. Intern. Organs* 34 (1988) 300.
- [29] G. Beaudoin, M.Y. Jaffrin, Plasma filtration in Couette flow membrane devices, *Artif. Organs* 13 (1989) 43.

- [30] K.H. Kroner, V. Nissinen, H. Ziegler, Improved dynamic filtration of microbial suspensions, *Bio/Technology* 5 (1987) 921.
- [31] K.H. Kroner, V. Nissinen, Dynamic filtration of microbial suspensions using an axially rotating filter, *J. Membr. Sci.* 36 (1988) 85.
- [32] S. Wronski, E. Molga, L. Rudniak, Dynamic filtration in biotechnology, *Bioprocess Eng.* 4 (1989) 99.
- [33] B. Hallström, M. Lopez-Leiva, Description of a rotating ultrafiltration module, *Desalination* 273 (1978) 24.
- [34] W. Tobler, Dynamic filtration—the engineering concept of the Escher Wyss pressure filter, *Filtr. Sep.* 15 (1979) 630.
- [35] H.B. Winzeler, G. Belfort, Enhanced performance for pressure-driven membrane processes: the argument for fluid instabilities, *Membr. Sci.* 80 (1993) 35.
- [36] A. Margaritis, C.R. Wilke, The rotorfermentor. I. Description of the apparatus, power requirements, and mass transfer characteristics, *Biotechnol. Bioeng.* 20 (1978) 709.
- [37] W. Tobler, Dynamic filtration: principle and application of shear filtration in an annular gap, *Filtr. Sep.* 19 (1982) 329.
- [38] T. Murase, E. Iritani, P. Chidphong, K. Kano, K. Atsumi, M. Shirato, High speed microfiltration using a rotating, cylindrical ceramic membrane, *Int. Chem. Eng.* 31 (1991) 370.
- [39] H.W. Müller, M. Liu, Structure of ferrofluid dynamics, *Phys. Rev. E* 64 (2001) 061405.
- [40] S. Odenbach, H.W. Müller, Stationary off-equilibrium magnetization in ferrofluids under rotational and elongational flow, *Phys. Rev. Lett.* 89 (2002) 037202.
- [41] S. Odenbach, *Magnetoviscous Effects in Ferrofluids*, volume m71 of *Lecture Notes in Physics*, Springer, Berlin, 2002.
- [42] S. Odenbach (Ed.), *Ferrofluids – Magnetically controllable Fluids and their Applications*, *Lect. Notes Phys.* vol. 594, Springer, Berlin, 2002.
- [43] S. Odenbach, H.W. Müller, On the microscopic interpretation of the coupling of the symmetric velocity gradient to the magnetization relaxation, *J. Magn. Magn. Mater.* 289 (2005) 242.
- [44] P. Langevin, Magnétisme et théorie des électrons, *Annales de Chemie et de Physique* 5 (1905) 70.
- [45] D. Martinand, E. Serre, R. Lueptow, Linear and weakly nonlinear analyses of cylindrical Couette flow with axial and radial flows, *J. Fluid Mech.* 824 (2017) 438.
- [46] A. Recktenwald, M. Lücke, H.W. Müller, Taylor vortex formation in axial through-flow: Linear and weakly nonlinear analysis, *Phys. Rev. E* 48 (1993) 4444.
- [47] G. Ahlers, D.S. Cannell, Vortex-front propagation in rotating Couette-Taylor flow, *Phys. Rev. Lett.* 50 (1983) 1583.
- [48] O. Czarny, E. Serre, P. Bontoux, R. Lueptow, Interaction between Ekman pumping and the centrifugal instability in Taylor-Couette flow, *Phys. Fluids* 15 (2003) 467.
- [49] D.-C. Kuo, K.S. Ball, Taylor-Couette flow with buoyancy: onset of spiral flow, *Phys. Fluids* 9 (1997) 2872.
- [50] V. Sobolik, B. Izrar, R. Lusseyran, S. Skali, Interaction between the Ekman layer and the Couette-Taylor instability, *Int. J. Heat Mass Transfer* 43 (2000) 4381.
- [51] T.A. DeRoquefort, G. Grillaud, Computation of Taylor vortex flow by a transient implicit method, *Comput. Fluids* 6 (1987) 259.
- [52] G. Pfister, I. Rehberg, Space-dependent order parameter in circular Couette flow transitions, *Phys. Lett.* 83A (1981) 19.
- [53] S. Altmeyer, C. Hoffmann, M. Heise, J. Abshagen, A. Pinter, M. Lücke, G. Pfister, End wall effects on the transitions between Taylor vortices and spiral vortices, *Phys. Rev. E* 81 (2010) 066313.
- [54] J. Embs, H.W. Müller, C. Wagner, K. Knorr, M. Lücke, Measuring the rotational viscosity of ferrofluids without shear flow, *Phys. Rev. E* 61 (2000) R2196.
- [55] J.E. Hart, Ferromagnetic rotating Couette flow: The role of magnetic viscosity, *J. Fluid Mech.* 453 (2002) 21.
- [56] B. Eckhardt, S. Grossmann, D. Lohse, Torque scaling in turbulent Taylor-Couette flow between independently rotating cylinders, *J. Fluid Mech.* 581 (2007) 221.